ELSEVIER

Journal of Applied Geophysics 47 (2001) 271–284

JOURNAL OF APPLIED GEOPHYSICS

www.elsevier.com/locate/jappgeo

Nonlinear inversion of borehole-radar tomography data to reconstruct velocity and attenuation distribution in earth materials

Chaoguang Zhou [a], Lanbo Liu [a,*], John W. Lane Jr. [b]

[a] *Department of Geology and Geophysics, University of Connecticut, 354 Mansfield Road, U-45, Storrs, CT 06269-2045, USA*
[b] *Branch of Geophysical Applications and Support, US Geological Survey, USA*

Accepted 8 May 2001

Abstract

A nonlinear tomographic inversion method that uses first-arrival travel-time and amplitude-spectra information from cross-hole radar measurements was developed to simultaneously reconstruct electromagnetic velocity and attenuation distribution in earth materials. Inversion methods were developed to analyze single cross-hole tomography surveys and differential tomography surveys. Assuming the earth behaves as a linear system, the inversion methods do not require estimation of source radiation pattern, receiver coupling, or geometrical spreading. The data analysis and tomographic inversion algorithm were applied to synthetic test data and to cross-hole radar field data provided by the US Geological Survey (USGS). The cross-hole radar field data were acquired at the USGS fractured-rock field research site at Mirror Lake near Thornton, New Hampshire, before and after injection of a saline tracer, to monitor the transport of electrically conductive fluids in the image plane.

Results from the synthetic data test demonstrate the algorithm computational efficiency and indicate that the method robustly can reconstruct electromagnetic (EM) wave velocity and attenuation distribution in earth materials. The field test results outline zones of velocity and attenuation anomalies consistent with the finding of previous investigators; however, the tomograms appear to be quite smooth. Further work is needed to effectively find the optimal smoothness criterion in applying the Tikhonov regularization in the nonlinear inversion algorithms for cross-hole radar tomography.

Keywords: Electromagnetic wave; Tomography; Velocity; Attenuation; Ray tracing; Nonlinear inversion; Borehole radar

1. Introduction

Travel-time tomography is widely used in geophysical studies (Brzostowski and McMechan, 1992; Zhang, 1997) to image subsurface velocity variation; however, only the first-arrival travel-time information is used as the input data with these methods. The addition of first-arrival amplitude and frequency data can provide information about attenuation properties that can increase understanding of the earth materials through which waves have propagated. For seismic waves, high-attenuation and low-velocity zones usually coincide (Vasco et al., 1996; Cormier and Li, 1998). Thus, if the seismic-velocity distribution is known, we also have a general idea of the attenuation distribution. For electromagnetic (EM) waves, however, the attenuation distribution is usu-

* Corresponding author. Tel.: +1-860-486-1388; fax: +1-860-486-1383.
E-mail address: lanbo@geol.uconn.edu (L. Liu).

0926-9851/01/$ - see front matter
PII: S0926-9851(01)00071-4

ally not related to the velocity distribution. The velocity of EM waves is sensitive to the amount of fluid in the medium but insensitive to the electrical conductivity of the fluid. On the other hand, the attenuation of EM waves is affected by the electrical conductivity. For example, both freshwater and seawater have relative dielectric constants of about 81 and radar-frequency EM waves propagate at about the same speed in both media; however, the electrical conductivity of freshwater is on the order of 10^{-2} S/m, whereas seawater is about 4 S/m. Thus, EM wave attenuation in seawater is about 400 times greater than that in freshwater. For this reason, in fractured bedrock, cross-hole radar surveys conducted before, during, and after injection of saline tracers have the potential to detect transmissive zones in the image plane (Ramirez and Lytle, 1986; Olsson et al., 1992; Lane et al., 1996, 2000).

Various methods have been used to image velocity and attenuation. Brzostowski and McMechan (1992) used simultaneous iterative reconstruction technique (SIRT) tomography to image velocity and attenuation through the use of travel-time and amplitude information; however, the accuracy of SIRT methods is limited because SIRT is a linear inversion method where the ray paths always remain straight lines. In contrast, nonlinear tomography methods, where curved ray paths are allowable, can produce results with higher accuracy, but require a great deal more computing time than linear inversion methods.

Vasco et al. (1996) developed a perturbation method for simultaneous inversion of seismic travel times and amplitudes for velocity and attenuation. An analytical function to model the source radiation pattern and the receiver coupling is used in this method; however, it is difficult to accurately determine the source radiation pattern and receiver coupling because of the variation of rock type and borehole geometry (Peng et al., 1993; Gibson, 1994).

This paper presents data analysis and nonlinear tomography inversion methods that can be used to jointly reconstruct velocity and attenuation distribution in earth materials without the need to estimate source radiation pattern, receiver coupling, geometric spreading, or transmission coefficient. Most of the computing time for the nonlinear tomography algorithm is consumed by ray tracing. However, the ray-path information used for the velocity tomography also can be used for the attenuation tomography. Thus, a tomography algorithm that reconstructs both velocity and attenuation does not require much more time than one that only reconstructs velocity.

2. Theory

2.1. Attenuation of electromagnetic waves for constant Q models

Attenuation of EM waves commonly is characterized by the loss tangent ($\tan\delta$), which is inversely proportional to the quality factor, Q, (Strick, 1970; Kjartansson, 1979; Bano, 1996; Noon et al., 1998)

$$Q = \frac{\pi f}{\alpha v} = \frac{\varepsilon'}{\varepsilon''} = \frac{1}{\tan\delta}, \tag{1}$$

where f is the frequency, α is the attenuation, v is the phase velocity, and ε' and ε'' are the real and imaginary parts of the effective dielectric permittivity ε, respectively. Usually, ε' and ε'' are frequency dependent; however, if the real and imaginary parts of the dielectric permittivity have the same frequency dependence, which is largely true for earth materials, Q is frequency independent. Eq. (1) is referred to as the constant Q model.

For a constant Q model, the dielectric permittivity is dependent on the angular frequency, ω (Joncsher, 1977; Bano, 1996),

$$\varepsilon(\omega) = \varepsilon_r\left(-i\frac{\omega}{\omega_r}\right)^{n-1}, \tag{2}$$

where $0 < n < 1$, ω_r is the reference angular frequency, and ε_r is a real constant with the dimension of the permittivity.

Eq. (2) can be written as

$$\varepsilon(\omega) = \varepsilon_r\left(\frac{\omega}{\omega_r}\right)^{n-1}\left(e^{-i\frac{\pi}{2}}\right)^{n-1}, \tag{3}$$

or

$$\varepsilon(\omega) = \varepsilon_r\left(\frac{\omega}{\omega_r}\right)^{n-1}\left[\sin\left(\frac{n\pi}{2}\right) + i\cos\left(\frac{n\pi}{2}\right)\right]. \tag{4}$$

In Eq. (4), both the real and imaginary parts of $\varepsilon(\omega)$ show the same dependence on frequency. Ex-

perimental measurements of the dielectric permittivity for some engineered materials also have shown that the real and imaginary parts have the same frequency dependence (Robert, 1996).

For electromagnetic waves, the complex wave number k is given by

$$k(\omega) = \beta(\omega) + i\alpha(\omega) = \omega\sqrt{\mu\varepsilon(\omega)}, \quad (5)$$

where α is the attenuation; β is the phase constant; and μ is the magnetic permeability. For most non-magnetic rocks, the magnetic permeability is equal to its value in free space. For lossless media, $\alpha = 0$ and the wave number becomes real. Although the value might be small, attenuation is present in almost all earth materials.From Eqs. (4) and (5),

$$k(\omega) = \frac{\omega}{v_0}\left(\frac{\omega}{\omega_r}\right)^{(n-1)/2}\left\{1 + i\tan\left[\frac{\pi}{4}(1-n)\right]\right\}, \quad (6)$$

furthermore,

$$v(\omega) = v_0\left(\frac{\omega}{\omega_r}\right)^{(1-n)/2}, \quad (7)$$

and

$$\beta(\omega) = \frac{\omega}{v(\omega)}$$

$$\alpha(\omega) = \frac{\omega}{v(\omega)}\tan\left[\frac{\pi}{4}(1-n)\right], \quad (8)$$

and

$$v_0 = \frac{1}{\sqrt{\mu\varepsilon_r}\cos\left[\frac{\pi}{4}(1-n)\right]}. \quad (9)$$

From Eq. (4), the relation between Q and n is given by

$$Q = \frac{\varepsilon'(\omega)}{\varepsilon''(\omega)} = \tan\left(\frac{n\pi}{2}\right), \quad (10)$$

or

$$n = \left[\frac{2}{\pi}\tan^{-1}(Q)\right]. \quad (11)$$

When $n = 1$, $Q = \infty$, which is the case for a pure dielectric; when $n = 0$, $Q = 0$, which is the case for a pure conductor. Most rocks have relatively low electrical conductivity, so it can be assumed that n is very close, but less than, to unity.

2.2. Velocity dispersion

In Eq. (7), the phase velocity changes with the frequency; therefore, there is dispersion as electromagnetic waves propagate. Velocity dispersion is a result of the frequency dependence of the real part of the dielectric permittivity. By contrast, the attenuation, or more strictly the absorption, results from the imaginary part of the dielectric permittivity. Numerical modeling was used to assess the effect of velocity dispersion in typical earth materials. For granite, Q ranges from 12 to 18 (Bano, 1996). However, a lower Q value of 10 (corresponding $n = 0.93655$) was used in the numerical modeling. If it can be demonstrated that the velocity dispersion is not significant for $Q = 10$, it should be even less significant for higher Q values.

The variation of the velocity with respect to frequency for a dispersive medium ($Q = 10$, or $n = 0.93655$, in Eq. (7)) in comparison with a non-dispersive medium ($n = 1$ in Eq. (7)) is shown in Fig. 1. The reference velocity and the reference frequency are 130 m/μs and 300 MHz, respectively. The non-dispersive medium has a constant velocity over the entire frequency range. In contrast, the phase velocity in the dispersive medium is higher when the frequency increases, and lower when the frequency decreases. In the time domain, the observable phenomenon associated with velocity dispersion is the broadening of EM pulses with increasing propagation distance. The numerical modeling results for $Q = 10$ shown in Fig. 1 indicate the phase velocity changes very little over a wide range in frequency, supporting the hypothesis that in similar situations, velocity dispersion can be ignored.

The velocity dispersion also can be estimated quantitatively. Let the reference frequency $f_0 = 300$ MHz for velocity v_0 (130 m/μs) and $f_1 = 100$ MHz for velocity v_1. From Eq. (7),

$$\frac{v_1}{v_0} = \left(\frac{100}{300}\right)^{(1-0.93665)/2} \approx 96.58\%. \quad (12)$$

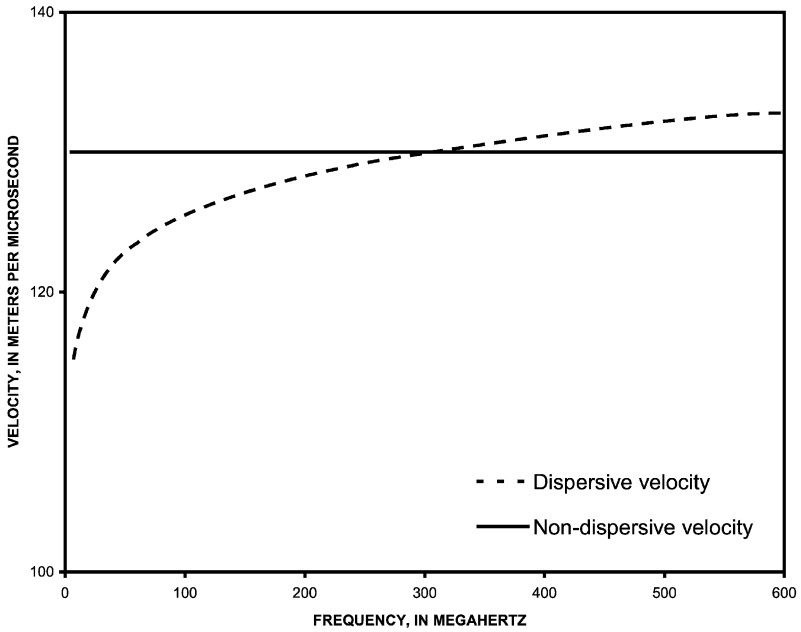

Fig. 1. Velocity dispersion of a wave with frequency centroid at 300 MHz and $Q = 10$. The variation of velocity is very small, especially in the area around the central frequency.

If the frequency is higher than the reference frequency, for example, $f_1 = 500$ MHz for velocity v_1 with the same reference frequency as above,

$$\frac{v_1}{v_0} = \left(\frac{500}{300}\right)^{(1-0.93665)/2} \approx 101.63\%. \quad (13)$$

For a Q value great than 10, the velocity dispersion is even smaller. Because the dispersion is so small within the frequency band of interest, velocity dispersion can be neglected. Thus, the rest of this paper concentrates on discussions of attenuation.

3. Attenuation tomography

3.1. Single-survey case

In the frequency domain, we assume the earth behaves as a linear system for propagating EM or seismic waves (Liu et al., 1998) as

$$R(\omega) = S(\omega)GP_S P_R T e^{-\int_L \alpha(\omega)\mathrm{d}s}, \quad (14)$$

where $R(\omega)$ is the response spectrum; $S(\omega)$ is the source spectrum; G is the geometric spreading factor; P_S and P_R are the source radiation pattern and receiver coupling, respectively; T is the effective transmission coefficient; and L is the integration path. G, P_S, P_R, and T are assumed to be independent of frequency.

Taking the natural log of both sides of Eq. (14) results in

$$\int_L \alpha(\omega)\mathrm{d}s = \ln S(\omega) + \ln G + \ln P_S + \ln P_R + \ln T - \ln R(\omega). \quad (15)$$

Taking the first derivative with respect to ω, G, P_S, P_R and T are eliminated from the equation

$$\int_L \frac{\mathrm{d}\alpha}{\mathrm{d}\omega}\mathrm{d}s = \frac{S'(\omega)}{S(\omega)} - \frac{R'(\omega)}{R(\omega)}. \quad (16)$$

Using Eq. (8),

$$\frac{\mathrm{d}\alpha}{\mathrm{d}\omega} = \frac{(n+1)\tan\left[\frac{\pi}{4}(1-n)\right]}{2v_0}\left(\frac{\omega}{\omega_r}\right)^{(n-1)/2} \quad (17)$$

$$= \frac{(n+1)\tan\left[\frac{\pi}{4}(1-n)\right]}{2v(\omega)}. \quad (18)$$

If the frequency dependence of velocity is neglected, the derivative of attenuation α with respect to ω is approximately constant. Equivalently, attenuation is a linear function of frequency, which is consistent with other investigations (Turner and Siggins, 1994; Bano 1996; Liu et al., 1998; Noon et al., 1998). Therefore,

$$\int_L m \mathrm{d}s = \Delta, \tag{19}$$

where

$$m = \frac{(n+1)\tan\left[\frac{\pi}{4}(1-n)\right]}{2v(\omega)}, \tag{20}$$

and

$$\Delta = \frac{S'(\omega)}{S(\omega)} - \frac{R'(\omega)}{R(\omega)}. \tag{21}$$

Both m and Δ are frequency dependent. At its centroid frequency, the derivative of the source spectrum is zero, and the first term on the right side of Eq. (21) disappears, which results in a much simpler equation. In this case, estimation of the source is not necessary and the tomography is much easier.

Eq. (19) will be used to invert for m, from which n and Q can be calculated. The equation does not include the geometric spreading, radiation pattern, or transmission coefficient. This method reduces computation time and errors in the calculation because these parameters are difficult to estimate accurately. In practice, the radiation pattern is very complicated. Although some theoretical studies have been conducted (Peng et al., 1993; Gibson, 1994; Arcone, 1995; Quan and Harris, 1997), it is difficult to account for the variations induced by changes in rock type and by transmitter and receiver coupling to the medium.

3.2. Repeated-survey case

Cross-hole radar tomography surveys have been coupled with the injection of electrically conductive tracers to support site characterization studies in fractured rock. Saline tracers increase EM attenuation; thus, attenuation-difference tomography can be used to locate transmissive fracture zones in the tomographic image plane (Lane et al., 1996). Usually, a baseline geophysical survey is conducted before the injection of the electrically conductive fluid tracer. During and (or) after the tracer injection, additional cross-hole surveys are conducted. These two data sets can be compared to identify attenuation differences induced by saline tracer in transmissive zones (Lane et al., 1996, 2000; Liu et al., 1998).

A linear system description of the earth before and after tracer injection is given by

$$R_1(\omega) = S(\omega) G P_S P_R T \mathrm{e}^{-\int_L \alpha 1(\omega)\mathrm{d}s}$$

$$R_2(\omega) = S(\omega) G P_S P_R T \mathrm{e}^{-\int_L \alpha 2(\omega)\mathrm{d}s}. \tag{22}$$

Taking natural logarithms to both sides results in

$$\int_L \alpha_1(\omega)\mathrm{d}s = \ln S(\omega) + \ln G + \ln P_S + \ln P_R + \ln T - \ln R_1(\omega)$$

$$\int_L \alpha_2(\omega)\mathrm{d}s = \ln S(\omega) + \ln G + \ln P_S + \ln P_R + \ln T - \ln R_2(\omega), \tag{23}$$

where the subscripts 1 and 2 denote the background and post-injection surveys, respectively. We assume changes in the received spectrum are induced by attenuation, rather than velocity changes. A simple difference of the two equations in Eq. (23) leads to

$$\int_L \delta\alpha \mathrm{d}s = \int_L (\alpha 2 - \alpha 1)\mathrm{d}s = \ln\left(\frac{R_1}{R_2}\right), \tag{24}$$

where $\delta\alpha$ is the change in attenuation between these two surveys. Regions with significant changes in attenuation are the flow paths of the highly transmissive zones.

Because the source radiation pattern, receiver coupling, transmission coefficients, and geometric spreading terms are not present in Eqs. (16) and (24), the data processing is much simpler. This simplification is attractive in terms of computational efficiency and the robustness of the tomographic reconstructions.

4. Nonlinear tomographic inversion for velocity and attenuation reconstruction

Eqs. (19) and (24) are in the same form as the equation for travel-time tomography,

$$\int_L \frac{1}{v}\,\mathrm{d}s = t, \tag{25}$$

where v is the phase velocity and t is the travel time. Eqs. (19), (24) and (25) can be written in the matrix form

$$\mathbf{G}(\mathbf{x}) = \mathbf{b}, \tag{26}$$

where $\mathbf{G}(\mathbf{x})$ is the integration with respect to model vector $\mathbf{x}$, and $\mathbf{b}$ is the data vector. For travel-time tomography, $\mathbf{x}$ is the slowness (the reciprocal of the velocity) and $\mathbf{b}$ is the travel-time; for the single-survey case, $\mathbf{x}$ is m and $\mathbf{b}$ is Δ; and for the repeated-survey case, $\mathbf{x}$ is $\delta\alpha$ and $\mathbf{b}$ is $\ln(R_1/R_2)$.

Eq. (26) is non-linear and underdetermined. For this paper, the Gauss–Newton method is used to linearize the equation and Tikhonov regularization (Tikhonov and Arsenin, 1977) is used to obtain a stable minimum-structure solution. The finite-difference travel-time calculation method developed by Zhou and Liu (1999) is used at each iteration step to update the ray paths.

Mathematically, a single matrix equation can be constructed for the inversion of velocity and attenuation (Vasco et al., 1996) in which the model vector $\mathbf{x}$ contains slowness and attenuation and the data vector $\mathbf{b}$ contains travel-times and amplitude information (Δ). Nevertheless, the approach used in this paper differs from Vasco et al. (1996) in two ways. First, it is more computationally efficient to solve two equation sets with smaller matrices and vectors than to solve a single, larger matrix equation. Second, because the regularization used in the inversion algorithm tends to smooth the solution, it is hard to justify the validity of smoothing slowness and attenuation to the same degree. This is because velocity and attenuation do not necessarily have the same distribution and heterogeneity scale. Therefore, at each iteration step of the tomography algorithms presented here, the ray paths are updated first, then a linearized matrix equation is solved for velocity, and finally the second linearized equation is solved for attenuation.

5. Material properties

Three major models are used to describe the effective complex dielectric property of earth materials (Robert, 1996): the Cole–Cole equation (Maxwell–Wagner), the double layer polarization equation, and the Debye equation. The first two models are more general and include a distribution of relaxation time τ:

$$\varepsilon(\omega) = \varepsilon'_\infty + \frac{\varepsilon'_s - \varepsilon'_\infty}{1 + (i\omega\tau)^{1-\alpha}} - i\frac{\sigma_0}{\omega\varepsilon_0},$$

(Cole–Cole) (27)

$$\varepsilon(\omega) = \varepsilon'_\infty + \frac{\varepsilon'_s - \varepsilon'_\infty}{1 + (2i\omega\tau)^{\beta} + i\omega\tau} - i\frac{\sigma_0}{\omega\varepsilon_0},$$

(double layer polarization), (28)

and the Debye model has a single relaxation time:

$$\varepsilon(\omega) = \varepsilon'_\infty + \frac{\varepsilon'_s - \varepsilon'_\infty}{1 + (i\omega\tau)} - i\frac{\sigma_0}{\omega\varepsilon_0},$$

(Debye effect), (29)

where ε'_s is the real dielectric permittivity at low frequency; ε'_∞ is the real dielectric permittivity at high frequency; σ_0 is the DC conductivity; and ε_0 is the dielectric permittivity in a vacuum. These theoretical models, even the simplest Debye model, show that the relaxation mechanisms cause the effective dielectric permittivity to decrease with frequency and the electrical conductivity to increase with frequency. These variations could be very complicated, because multiple relaxation frequencies are present, depending on how thoroughly the relaxation mechanisms are accounted for. Annan (1996) discussed the complexity of EM radar-wave dispersion arising from different combinations of transition frequency and relaxation frequencies.

If the relaxation mechanisms are completely neglected, i.e., the relaxation time approaches infinity, or equivalently, the static dielectric permittivity, ε'_s approaches the high frequency limit ε'_∞, all three equations reduce to an identical equation

$$\varepsilon(\omega) = \varepsilon' - i\frac{\sigma_0}{\omega\varepsilon_0}. \tag{30}$$

Eq. (30) shows that the imaginary part of the effective complex dielectric permittivity comes from the electrical conductivity, and the real part is independent of frequency. As discussed previously, the velocity dispersion is insignificant; therefore, it is natural to conclude that the real component of the dielectric permittivity dispersion is insignificant. For ideal dielectric materials, the velocity and attenuation can be approximated by their high frequency limits (Balanis, 1989; Annan, 1996):

$$v_\infty = \frac{1}{\sqrt{\mu\varepsilon'}}, \quad \alpha_\infty = \frac{\sigma}{2}\sqrt{\frac{\mu}{\varepsilon'}}. \tag{31}$$

To estimate the dielectric permittivity and the electrical conductivity, we then have

$$\varepsilon' = \frac{1}{\mu v_\infty^2} \quad \sigma = \frac{2\alpha_\infty}{\mu v_\infty}. \tag{32}$$

Eq. (32) is used later to estimate the dielectric constant and the electrical conductivity in the field experiment section (Section 6.2).

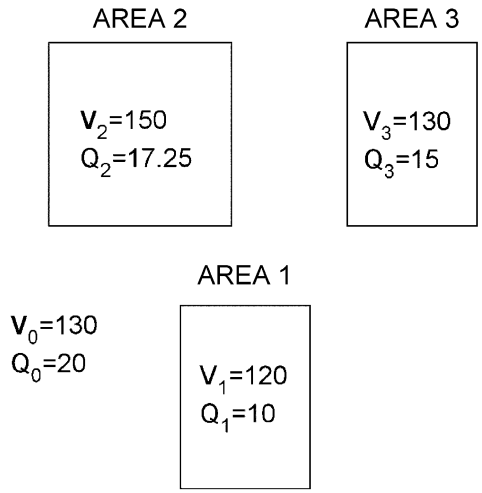

Fig. 2. The synthetic model used for testing the single-survey tomography method. The whole plane covers a 105×105-m^2 area and contains three anomalies with Q values of 10, 17.25, and 15. Only two areas (Area 1, the lower rectangular area, and Area 2, the upper left square) have velocities (in the unit of m/μs) different from the background. Area 3 (Upper right rectangular area) has a different Q value but the same velocity as the background. There are 25 source/receivers at equally spaced positions deployed on all four sides of the model. For a particular source, 24 receivers are located on the same side and 25 receivers are located on each of the other three sides. The total data set contains 100×99 traces.

6. Experiments

6.1. Tests of the single-survey data analysis and inversion algorithm with synthetic data

The data analysis and inversion algorithm presented in this paper were tested using synthetic data. The synthetic data test corresponds to reconstruction of velocity and Q from a single cross-hole tomography. The synthetic first-arrival times were generated with the use of the finite-difference technique of Zhou and Liu (1999). A 5% random noise was added to the synthetic travel times and amplitudes to approximate simulate cross-hole data obtained under field conditions. The model of velocity and Q used to generate the synthetic data is shown in Fig. 2. Three low Q anomalies are present, with the relative changes of 12.5%, 25%, and 50% from the original background value of 20. Two of the three anomalous areas have a velocity change (7.7% and 15.4%) relative to the background. The third area (Q with a 25% change) has the same velocity as the background. Unlike a typical field survey, the receivers are around all four sides of the model area, with 25 source/receiver positions on each side. For each source, 99 receivers record travel-time and amplitude information.

Assuming no a priori information about the structural features of the study area, the initial model is uniform and does not contain any velocity or Q anomalies. The initial values of velocity and Q are 130 m/μs and 20, respectively. Five iterations were needed to reconstruct the velocity and Q values shown in Figs. 3 and 4. Although the overall anomalies are reconstructed quite reasonably, two features can be noticed in the velocity reconstruction. First, the velocity anomaly of Area 2 (the upper left bright portion) has been clearly reconstructed. In contrast, the velocity anomaly of Area 1 (the lower center darker portion) is reconstructed with larger inaccuracies in the velocity value and the anomaly boundary.

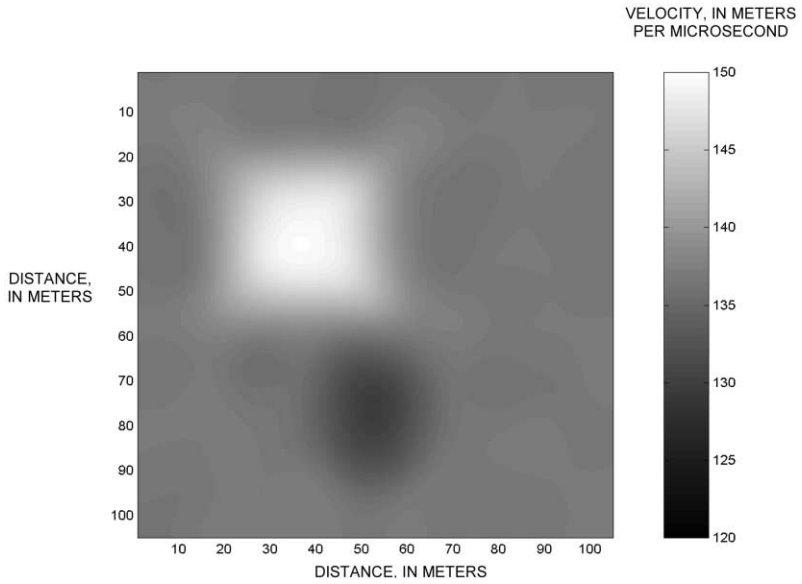

Fig. 3. Velocity tomogram reconstructed for the model shown in Fig. 2. The velocity anomaly of Area 2 (the upper left bright portion) has been clearly reconstructed. The inverted velocity value is consistent with the model value of 150 m/μs. In contrast, the velocity anomaly of Area 1 (the lower center darker portion) is reconstructed with higher inaccuracies in both the velocity value and the anomaly boundary. This anomaly probably is caused by the fact that Area 1 is smaller in area and lower in velocity.

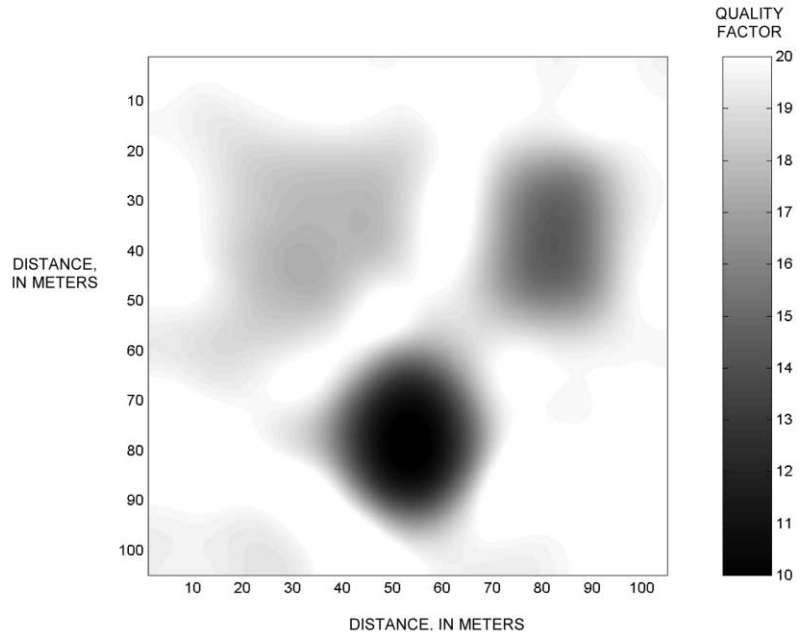

Fig. 4. Quality factor tomogram of the synthetic model. All three Q anomalies are well reconstructed and the values are well matched with the model.

This probably is because Area 1 is smaller in area and lower in velocity contrast. Second and more importantly, Area 1 is a low-velocity anomaly; diffraction degradation makes the image of the low velocity area smaller than its actual size, and diffraction healing makes it difficult to detect low velocity anomalies (Gheshlaghi and Santamarina, 1998). Furthermore, the term for model roughness penalty (the Tikhonov regularization) used in the inversion algorithm tends to smear out and suppress the short wavelength anomalies because some of these features are artifacts caused by poor coverage of ray paths in this area.

6.2. Cross-hole radar field data

The cross-hole data analysis and tomographic inversion algorithms presented in this paper were tested using cross-hole radar data from the USGS fractured-rock research site at Mirror Lake within the US Forest Service Hubbard Brook Experimental Forest, Grafton County, New Hampshire (Lane et al., 1996). In this area, the fracture orientation is highly variable, and the fracture system is poorly connected. This suggests that fluid flow in the fracture system is heterogeneous, tortuous, and flows in highly channeled flow paths (Lane et al., 1996). Fracture mineralization includes iron oxide coatings on fracture surfaces that have penetrated as much as 1 m into the bedrock. These iron oxide precipitates may induce halos of high electrical conductivity surrounding transmissive zones. Cross-hole radar data acquired in four boreholes within the Forest Service East (FSE) well field (FSE 1–4) were used for this study (Fig. 5a). Two hydraulically conductive zones connecting the four boreholes are shown in Fig. 5b (Lane et al., 1996).

A series of borehole-radar experiments previously were conducted at the site (Fig. 5a) to test the use of borehole-radar methods to detect saline tracers in fractured rock (Lane et al., 1999). The experimental procedure used to acquire the field data analyzed in this paper is described by Lane et al. (1996). Briefly, saline solution with NaCl concentrations of 20 to 28 g/l was injected into well FSE-1 and pumped out from FSE-4. During injection, packers were used to isolate the zone from 40 to 50 m in the injection well. Cross-hole radar surveys using 60-MHz antennas were conducted before and after injection, with the transmitting antenna in well FSE-3 and the receiving antenna in well FSE-2. The data were collected at depths of 20 to 70 m at 2-m intervals.

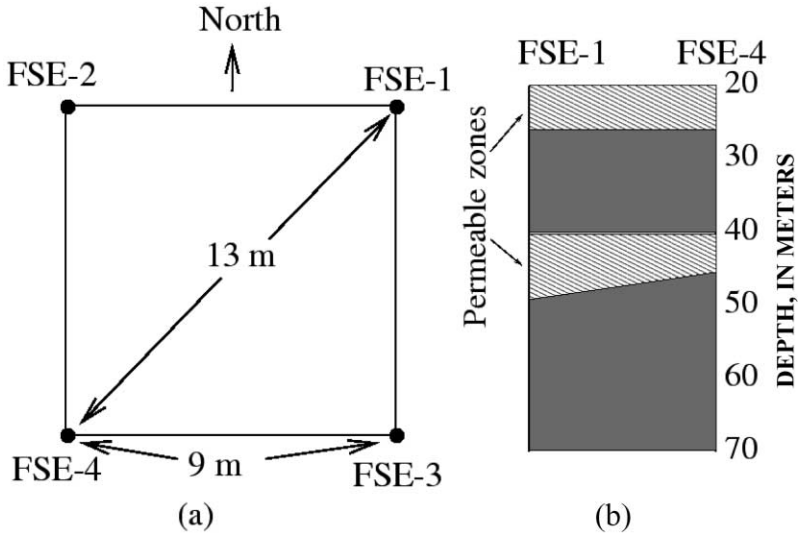

Fig. 5. (a) Map view of the wells at Mirror Lake test site. (b) The sketch of cross-section between FSE-1 and FSE-4. Saline water was injected from well FSE-1 and pumped out from well FSE-4. The injection zone between 40 and 50 m was isolated by packers. Cross-hole radar surveys were performed between wells FSE-2 and FSE-3 (after Lane et al., 1996).

Sample cross-hole radar records acquired before and after the injection are shown in Fig. 6. The rated central frequency of impulse radar antennas typically is based on measurements in air. When impulse radar antennas are used under real-world conditions and coupled with earth materials, the frequency of the received signal will be shifted down to a lower central frequency. This is known as frequency loading. For materials with a dielectric constant in the range 1–15, the value of the loaded frequency, f_L, i.e., the signal frequency upon coupling with the earth material, can be expressed as (Rashkovskij, 1981)

$$f_L = \frac{f_0}{\sqrt{\frac{2}{1+\frac{1}{\varepsilon_r}}}}. \quad (33)$$

If the nominal antenna frequency, f_0, is 60 MHz, and the antenna is used in granite with a dielectric constant of about 5 to 6, the loaded frequency is about 45 to 46 MHz. A value of 45 MHz as the centroid of the loaded frequency is used in estimat-

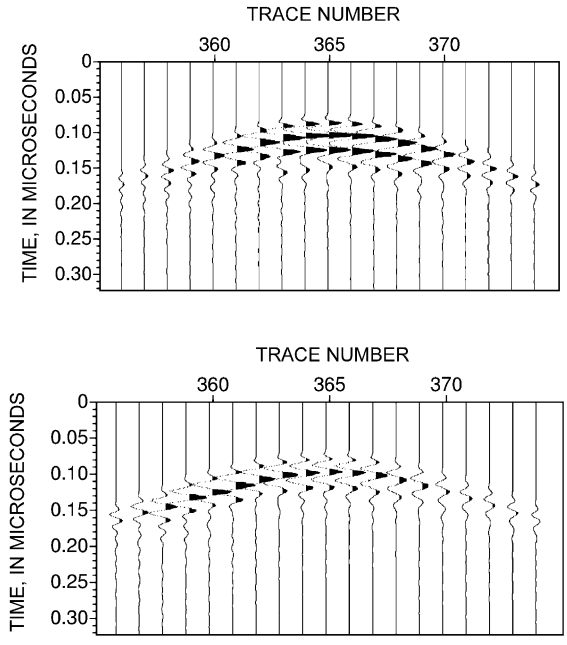

Fig. 6. Example of the cross-hole radar records at the FSE well field for trace numbers 352 to 379. Upper panel: before injection of the saline tracer; Lower panel: after injection of the saline tracer. Note the loss of amplitude after injection.

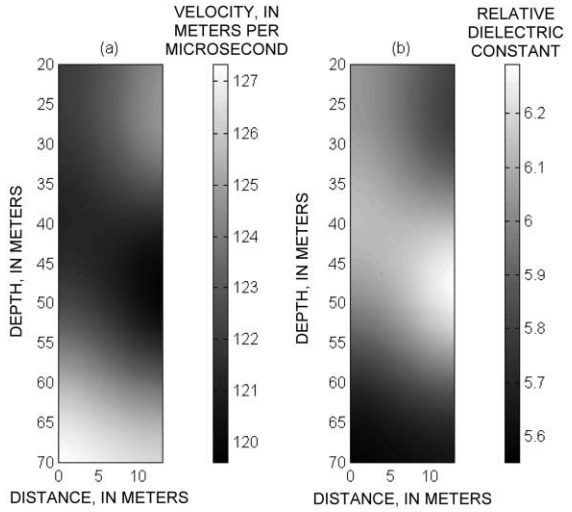

Fig. 7. (a) Reconstructed velocity tomogram between wells FSE-2 and FSE-3. (b) Computed relative dielectric constant distribution between wells FSE-2 and FSE-3. The slightly lower velocity (higher dielectric constant) zone in the middle of the profiles could be a result of higher water content because of the increased fracture density or porosity.

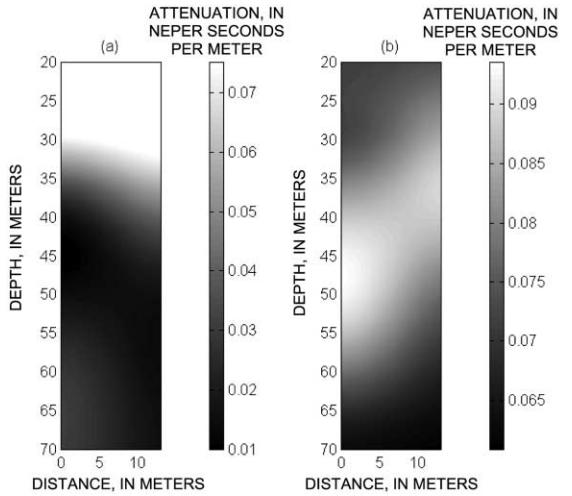

Fig. 8. Attenuation tomograms between wells FSE-2 and FSE-3. (a) Background attenuation. The high attenuation in the top zone suggests iron-oxide precipitates from the surface (Lane et al., 1996). (b) Attenuation after injection. Strong attenuation in the middle correlates to the lower hydraulically conductive zone.

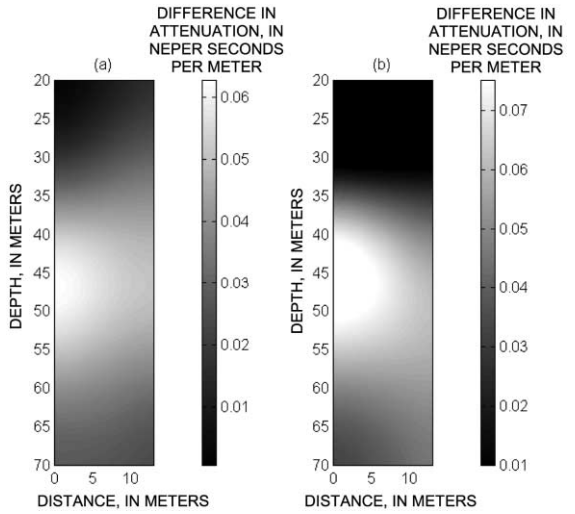

Fig. 9. (a) Differential attenuation tomogram reconstructed using the repeated-survey method. (b) Difference tomogram between the distributions of Fig. 8a,b. In general, a good coincidence is present between these two images.

ing $S(\omega)$. All the data processing in tomogram reconstruction (Figs. 7–11) was conducted at a frequency of 45 MHz.

6.3. Cross-hole velocity and attenuation tomograms

The single-survey method was applied to the data collected before and after injection to obtain background tomograms and post-injection tomograms. The repeated method also was used to reconstruct the differential attenuation tomogram between these two surveys. The reconstructed velocity and relative dielectric constant images are shown in Fig. 7. The images show little variation, consistent with interpretation of core sample lithology (Johnson and Dunstan, 1998). A slight low velocity zone is present at a depth of 45 m, probably because of the elevated porosity in the lower hydraulically conductive zone. Reconstructed attenuation distributions from before

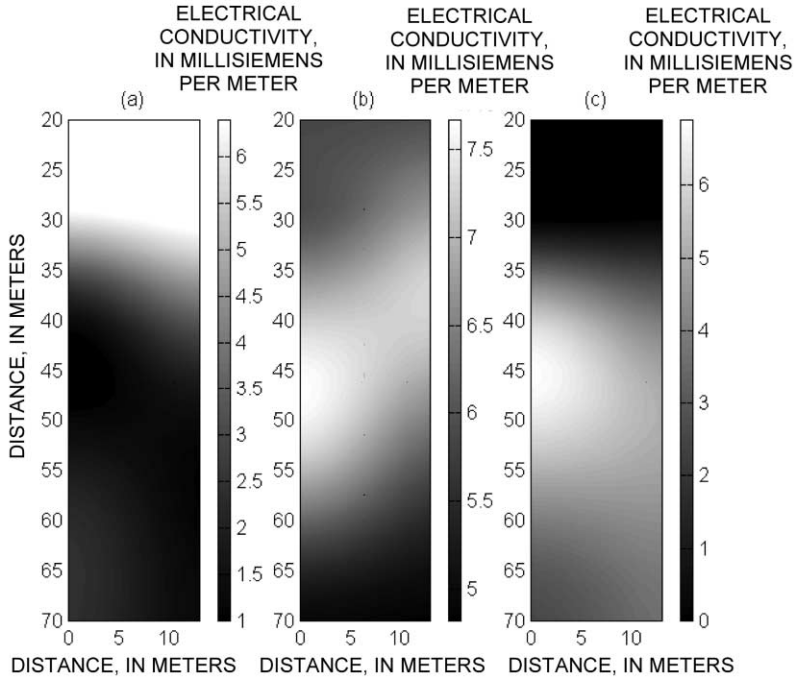

Fig. 10. Distribution of electric conductivity. (a) Before injection; (b) after injection; and (c) difference of (a) and (b). The strong conductivity change near the depth of 45 m coincides with the lower hydraulically conductive zone.

and after the saline injection are shown in Fig. 8. In general, these attenuation tomograms are consistent with the results obtained by Lane et al. (1996) using a linear tomography algorithm. The pre-injection background data (Fig. 8a) shows a high-attenuation zone that correlates with the upper hydraulically conductive zone at depths of 20 to 25 m, indicating that conductive minerals or iron compounds are present in the upper transmissive zone. The data do not display any high value for the lower hydraulically conductive zone at a depth of about 45 m. In contrast, the tomogram of the post-injection data (Fig. 8b) shows a strong attenuation zone that coincides with the lower hydraulically conductive zone. The area of highest attenuation is near well FSE-2, which shows that the fracture density and connectivity possibly are high near well FSE-2. Geological studies indicate that the majority of fractures strike to the northeast, with dips greater than 45° (Lane et al., 1996). The interconnection between these dipping fractures may control the connectivity and flow of saline water between the wells. The attenuation-difference tomogram calculated using the repeated-survey method is shown in Fig. 9a. The difference tomogram computed by differencing the attenuation distributions shown in Fig. 8b and a, which were computed by the single-survey method before and after the saline tracer injection, is shown in Fig. 9b. The images shown in Fig. 9 from the single-survey and repeated-survey methods are consistent and both clearly show the hydraulically conductive zone at about a depth of 45 m. Fig. 9 also shows that the area with high attenuation change is not in the center as expected, which indicates the main flowpath is not straight. This is consistent with the fracture geology in the bedrock (Lane et al., 1996) and the results obtained by the centroid-frequency downshift method (Liu et al., 1997, 1998). The computed electrical conductivity distributions are displayed in Fig. 10, which shows the conductivity change between the two surveys. The maximum change in electrical conductivity is about 8 mS/m. The Q distributions (Fig. 11) indicate a decrease to 1.5 near the hydraulically conductive zone at a depth of about 45 m after injection of the saline tracer. The difference tomogram in Fig. 11c also shows that the attenuation mostly changed in the hydraulically conductive zone at a depth of about 45 m.

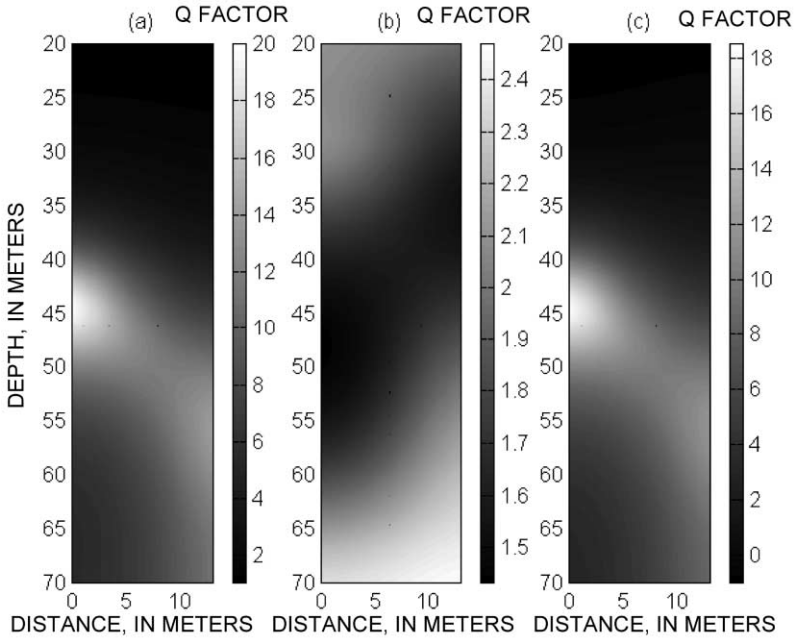

Fig. 11. Q tomograms. (a) Before injection; (b) after injection; and (c) difference of (a) and (b). The injection of saline water causes decrease of Q values in the hydraulically conductive zone at the depth of about 45 m.

7. Summary and conclusions

Two cross-hole radar data analysis and nonlinear tomography methods were developed to jointly invert first-arrival travel-time and amplitude-spectra data to reconstruct velocity and attenuation distribution. Neither method requires knowledge of the source radiation pattern nor receiver coupling. Not requiring this knowledge is advantageous because it is hard to accurately estimate radiation pattern and receiver/medium coupling for field conditions. A single-survey method can be used to image the velocity and attenuation of earth media, whereas a repeated-survey method can be used to monitor changes in attenuation concurrent with injection of electrically conductive tracers. The data-analysis methods and tomographic inversion algorithm were tested on synthetic and field data. The synthetic data-test results demonstrate the inversion algorithm computational efficiency, and indicate the proposed data analysis methods can be used to robustly reconstruct electromagnetic velocity and attenuation distribution in earth materials. The field data test results outline zones of velocity and attenuation anomalies consistent with the finding of previous investigators. Experimental results also indicate that the single-survey method can be used to detect velocity and attenuation anomalies and to infer the dielectric permittivity and electrical conductivity of the earth materials. Differential survey analysis methods can be used to identify attenuation differences induced by injection of saline tracer into transmissive zone in the tomographic image plane. However, the tomograms appear to be excessively smooth and further work is needed to reduce the damping effects of the algorithm cost function.

Acknowledgements

Computing facilities used in this study were partially supported by the National Science Foundation (NSF-EAR-9712012). The Hubbard Brook Experimental Forest is operated and maintained by the Northeastern Forest Experiment Station, USDA Forest Service, Radnor, Pennsylvania. The authors are grateful to USGS personnel Jared Abraham, Marc Buursink, Peter Joesten, Barbara Korzendorfer, W.M. Alley, Angel Martin, and Alison Waxman for their constructive suggestions, and thorough and critical reviews during the preparation and revision of the manuscript. The comments made by two anonymous reviewers and the Guest Editors greatly improved the readability of this paper.

References

Annan, A.P., 1996. Transmission dispersion and GPR. J. Environ. Eng. Geophys. 0, 125–136.

Arcone, S.A., 1995. Numerical studies of the radiation patterns of resistively loaded dipoles. J. Appl. Geophys. 33, 39–52.

Balanis, C.A., 1989. Advanced Engineering Electromagnetics. Wiley, New York, 981 pp.

Bano, M., 1996. Constant dielectric losses of ground-penetrating radar waves. Geophys. J. Int. 124, 279–288.

Brzostowski, M.A., McMechan, G.A., 1992. 3-D tomographic imaging of near-surface seismic velocity and attenuation. Geophysics 57, 396–403.

Cormier, V.F., Xu, L., 1998. Seismic attenuation of the inner core: viscoelastic or stratigraphic? Geophys. Res. Lett. 25, 4019–4022.

Gheshlaghi, F., Santamarina, J.C., 1998. Data pre-processing in cross-hole geotomography. J. Environ. Eng. Geophys. 3, 41–47.

Gibson, R.L., 1994. Radiation from seismic sources in cased and cemented boreholes. Geophysics 59, 518–533.

Johnson, C.D., Dunstan, A.H., 1998. Lithology and fracture characterization from drilling investigations in the Mirror Lake area, Grafton County, New Hampshire. U.S. Geological Survey Water-Resources Investigations Report 98-4183, 211 pp.

Joncsher, A.K., 1977. The 'universal' dielectric response. Nature 267, 673–679.

Kjartansson, E., 1979. Constant Q wave propagation and attenuation. J. Geophys. Res. 84, 4737–4748.

Lane Jr., J.W., Haeni, F.P., Placzek, G., Wright, D.L., 1996. Use of borehole-radar methods to detect a saline tracer in fractured crystalline bedrock at the mirror lake site, Grafton County, New Hampshire. Proceedings of the Sixth International Conference on Ground Penetrating Radar (GPR 96), pp. 185–190.

John Jr., J.W., Wright, D.L., Haeni, F.P, 1999. Borehole radar tomography using saline tracer injections to image fluid flow in fractured rock. U.S. geological toxic substances hydrology program. In: Morganwalp, D.W., Buxton, H.T. (Eds.), Proceedings of the Technical Meeting. USGS Water-Resources Investigations Report 99-4018C, vol. 3, pp. 747–756.

Lane Jr., J.W., Day-Lewis, F.D., Harris, J.M., Haeni, F.P., Gorelick, S.M., 2000. Attenuation-difference radar tomography: results of a multiple-plan experiment at the U.S. geological survey fractured rock research site, mirror lake, New Hampshire. In: Noon, D.A., Stickley, G.F., Longstaff, D. (Eds.),

Proceedings of the Eighth International Conference on Ground Penetrating Radar (GPR 2000), pp. 666–675.

Liu, L., Zhou, C., Lane Jr., J.W., Haeni, F.P., 1997. Cross-hole radar attenuation tomography using a frequency centroid down-shift method: consideration of non-linear frequency dependency of EM wave attenuation. Expanded Abstracts, the 67th Annual Meeting of Society of Exploration Geophysicists, pp. 442–445.

Liu, L., Lane Jr., J.W., Quan, Y., 1998. Radar attenuation tomography using the frequency downshift method. J. Appl. Geophys. 40, 105–116.

Noon, D.A., Stickley, G.F., Longstaff, D., 1998. A frequency-independent characterization of GPR penetration and resolution performance. J. Appl. Geophys. 40, 127–137.

Olsson, O., Anderson, P., Carlsten, S., Falk, L., Niva, B., and Sandberg, E., 1992. Fracture characterization in crystalline rock by borehole radar. Ground Penetrating Radar, J. Pilon (ed.), Geological Survey of Canada Paper 90-4, 139–150.

Peng, C., Cheng, C., Toköz, M.N., 1993. Borehole effects on downhole seismic measurements. Geophys. Prospect. 41, 883–912.

Quan, Y., Harris, J.M., 1997. Seismic attenuation tomography using the frequency shift method. Geophysics 62, 895–905.

Ramirez, A.L., Lytle, R.J., 1986. Investigation of fracture flow paths using alterant geophysical tomography. J. Rock Mech. Min. Sci. Geomech. 23, 165–169.

Rashkovskij, S.L., 1981. Linear vibrator characterizations near the boundary of two mediums. Radio Phys. 24 (4) (in Russian).

Robert, A., 1996. Dielectric permittivity of concrete between 50 MHz and 1 GHz and GPR measurements for building materials evaluation. Proceedings of the Sixth International Conference on Ground Penetrating Radar (GPR 96), pp. 117–122.

Strick, E., 1970. A predicted pedestal effect for pulse propagation in constant-*Q* solids. Geophysics 35, 387–404.

Tikhonov, A.N., Arsenin, V.Y., 1977. Solutions of Ill-Posed Problems. V.H Winston and Sons, Washington, DC, 258 pp.

Turner, G., Siggins, A.F., 1994. Constant-*Q* attenuation of subsurface radar pulses. Geophysics 59, 1192–1200.

Vasco, D.W., Peterson Jr., J.E., Majer, E.L., 1996. A simultaneous inversion of seismic traveltimes and amplitudes for velocity and attenuation. Geophysics 61, 1738–1757.

Zhang, J., 1997. Non-linear refraction and reflection traveltime tomography. PhD thesis, Massachusetts Institute of Technology, 252 pp.

Zhou, C., Liu, L., 1999. First arrival time calculation in 3-D media using finite difference method. Expanded Abstracts, 69th Annual Meeting of Society of Exploration, pp. 1406–1409.